energies

MDPI

Article

Solar Irradiance Ramp Classification Using the IBEDI (Irradiance-Based Extreme Day Identification) Method

Llinet Benavides Cesar * and Oscar Perpiñán-Lamigueiro

Departamento de Ingeniería. Eléctrica, Electrónica, Automática y Física Aplicada, Escuela Técnica Superior de Ingeniería y Diseño Industrial (ETSIDI), Universidad Politécnica de Madrid (UPM), 28012 Madrid, Spain; oscar.perpinan@upm.es

* Correspondence: llinet.bcesar@upm.es

Abstract: The inherent variability of solar energy presents a significant challenge for grid operators, particularly when it comes to maintaining stability. Studying ramping phenomena is therefore crucial to understanding and managing fluctuations in power supply. In line with this goal, this study proposes a new classification approach for solar irradiance ramps, categorizing them into four distinct classes. We have proposed a methodology including adaptation and extension of a wind ramp classification to solar ramp classification titled the Irradiance-Based Extreme Day Identification method. Our proposal includes an agglomerative algorithm to find new ramp class boundaries. The strength of the proposed method relies on that it allows its generalization to any dataset. We assessed it on three datasets from distinct geographic regions—Oregon (northwestern United States), Hawaii (central Pacific Ocean), and Portugal (southwestern Europe)—each with varying temporal resolutions of five seconds, ten seconds, and one minute. The class boundaries for each dataset results in different limits of Z score value, as a consequence of the different climatic characteristics of each location and the time resolution of the datasets. The "low" class includes values less than 0.62 for Portugal, less than 2.17 for Oregon, and less than 2.19 for Hawaii. The "moderate" class spans values from 0.62 to 3.51 for Portugal, from 2.17 to 5.01 for Oregon, and from 2.19 to 5.88 for Hawaii. The "high" class covers values greater than 3.51 and up to 6 for Portugal, greater than 5.01 and up to 10.72 for Oregon, and greater than 5.88 and up to 8.01 for Hawaii. Lastly, the "severe" class includes values greater than 6 for Portugal, greater than 10.72 for Oregon, and greater than 8.01 for Hawaii. Under cloudy sky conditions, it is observed that the proposed algorithm is able to classify the four classes. These thresholds show how the proposed methodology adapts to the unique characteristics of each regional dataset.

Keywords: solar ramps classification; solar irradiance; photovoltaics; agglomerative clustering

Academic Editor: Philippe Leclère

Received: 14 November 2024
Revised: 29 December 2024
Accepted: 5 January 2025
Published: 8 January 2025

Citation: Benavides Cesar, L.; Perpiñán-Lamigueiro, O. Solar Irradiance Ramp Classification Using the IBEDI (Irradiance-Based Extreme Day Identification) Method. *Energies* **2025**, *18*, 243. https://doi.org/10.3390/en18020243

1. Introduction

The increasing integration of renewable energy sources into electricity systems presents significant challenges for grid operators. Among these challenges, variability and uncertainty in solar power generation are major obstacles to maintain the stability and reliability of the electricity supply [1]. Solar irradiance ramp events, which are characterized by abrupt changes in energy production, are particularly difficult to forecast and manage.

The analysis generally used in the study of ramps to address their negative impact is a binary classification method (ramp/no ramp) based on a threshold, which is defined according to the magnitude and duration of the event [2]. There are different strategies

to attack the ramping problem, devices in the network [3], forecast algorithms [4], post-processing tools [5], etc.

In [3], the authors proposed to optimized solar photovoltaic power generation, affected by climatic variations, by improving the energy storage system. To achieve this, they analyzed the ramps, classifying them as ascending and descending ramps. The system remains active only during descending ramps, providing time for recovery and enhancing its responsiveness. They state that the challenge is to find the power ramp rate limit that achieves balance in the network. For their particular case, they varied it dynamically.

Other authors who have addressed the binary classification of ramps are [6–8]. In [6], Wellby et al. classified ramps as positive and negative following an evaluation of different extreme climatic conditions. Abuella et al. [7] evaluated a set of machine learning methods to classify ramps as either up or down, and subsequently categorize each classification as low or high. They use up to 15 features as input to the models, selecting subsets of features specific to each algorithm, with the series of calculated ramps being the only feature consistently used across all methods.

Previous research, such as the study by Eltohamy et al. [9] on wind power ramps, has shown that these events have a considerable impact on the flexibility required to balance supply and demand in power systems with high renewable energy penetration. However, most previous studies have focused on binary classifications or arbitrary classification methods that do not fully capture the complexity and diversity of these events [10,11]. In addition, there is no clear consensus on the definition and categorization of ramps [2,8], which makes it difficult to compare results between different research.

In [9], the authors have proposed a new technique for classifying power ramps based on a standard deviation score. In this way, ramps are classified according to this score into low, moderate, high, and severe. This technique has been evaluated for wind data, but the authors state that it is generalizable to solar data.

This research performs a critical analysis of the method proposed in [9], evaluating weaknesses found in its implementation to classify irradiance ramps: (1) the authors did not define the criteria followed to establish the limits of the classes; (2) the cause for labeling the classes as low, moderate, high, and severe is not determined; and (3) using the proposed value limits given by the authors, a class remains empty. From this analysis, we introduce an improvement to identify the boundaries for the classes, adding to the classification procedure a clustering method with the aim of establishing new limits, which better fit the classification of solar irradiance ramps.

The contributions of this study are as follows:

1. A new methodology for the classification of solar irradiance ramps is proposed: the Irradiance-Based Extreme Day Identification method.
2. The proposed method has its strength in the agglomerative clustering algorithm that allows its generalization to any dataset.
3. Impact assessment is carried out on three different time resolution datasets, two of which are public and could be used for comparison.

The document is structured in sections. Section 2 describes in detail the proposed methodology, including the clustering algorithm and the standard deviation scoring technique used. Section 3 focuses on datasets used in this paper. Section 4 outlines the results obtained applying this methodology to real solar irradiance datasets, evaluating its effectiveness and accuracy and Section 5 addresses a comparison between all results. Section 6 presents conclusions and suggestions for future research.

2. Materials and Methods

The method proposed in [9] called "Power ramp classification technique based on standard deviation score" is described first.

2.1. Power Ramp Classification Technique Based on Standard Deviation Score

For a time interval identified as Δt, the power ramps, Δp_n, of the historical N measurements of the series are calculated as shown in Equation (1).

$$\Delta p_n = P(t_n + \Delta t) - P(t_n), n = (1, \ldots\ldots, N) \quad (1)$$

The ramps are classified as ascending $\Delta p \uparrow$ or descending $\Delta p \downarrow$ according to their positive or negative value and are counted. The symbol n_+ represents the number of ascending ramps and the symbol n_- represents the number of descending ramps. Only the equations for the calculations with ascending ramps are shown; for descending ramps, they would be similar equations changing to the symbols n_- and $\downarrow$.

Next, the average number of ascending ramps and the average number of descending ramps are calculated separately in Equation (2).

$$\Delta p_{avg} \uparrow = \frac{1}{n_+} \sum_{i=1}^{n_+} \Delta p \uparrow (i) \quad (2)$$

The standard deviation of the ascending and descending ramps is calculated also for each particular case as shown in Equation (3).

$$\sigma_t \uparrow = \sqrt{\frac{1}{n_+ - 1} \sum_{i=1}^{n_+} \left(\Delta p \uparrow (i) - \Delta p_{avg} \uparrow\right)^2} \quad (3)$$

The standard deviation score is represented by Z and calculated as shown in Equation (4).

$$Z \uparrow (i) = \frac{\left(\Delta p \uparrow (i) - \Delta p_{avg} \uparrow\right)}{\sigma_t \uparrow} \quad (4)$$

Finally, the limits proposed by the authors on the Z values are applied to find the classes. The ramps with Z values below zero belong to the low classification, the moderate class includes values between 0 and 1, the high class includes values between 1 and 2, and the severe class includes values greater than 2.

The method based on standard deviation score can be summarized by the following Algorithm 1:

Algorithm 1. Original standard deviation score procedure

1. Calculate the ramps
2. Quantify the ascending and descending ramps.

For ascending ramps calculate:
- Average
- Standard deviation
- Standard deviation score

For downward ramps calculate:
- Average
- Standard deviation
- Standard deviation score

3. Rank the ramps according to the limits set by the authors for the absolute value of the standard deviation score.

The algorithm starts by calculating the ramps using a time series of irradiance. For each pair of values, the difference between the irradiance at the current time step and the previous one is calculated, with the time interval between the two values (e.g., 10 s) being considered for each subtraction, and this process is repeated for the entire series. Then, the ramps are quantified and denoted into ascending and descending ramps. For each of these groups of ramps, the average and the standard deviation are calculated, and the score based on the standard deviation Z is computed. Each of the ramps obtained in the first step has associated a Z score value after that step. The absolute value of these values is calculated. As a last step, the ramps are classified using the limits set by the authors into the four defined classes (low, moderate, high, and severe).

2.2. Problems Encountered in Its Application to Solar Irradiance

When applying the method described in the previous section to global irradiance values, it was found that (1) the authors did not define the criteria followed to establish the limits of the classes used in step 3 of the algorithm; (2) the cause for labeling the classes as low, moderate, high, and severe was not determined; and (3) using the proposed value limits given by the authors, a class remains empty. Figure 1 shows an example of the classification produced by this method, where the green color represents the low class, the orange color the high class, and the red color the severe class. In this figure only, three classes can be distinguished, because the moderate class is unrepresented. This problem can be observed in most of the time series we have analyzed.

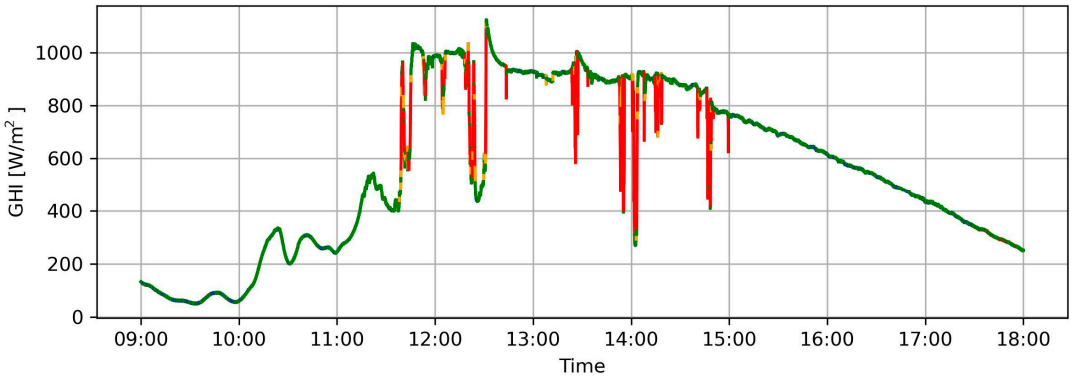

Figure 1. Classes obtained from the irradiance ramps after applying the method based on standard deviation on the data of one day. Note: The green color represents the low class, the orange color the high class, and the red color the severe class.

2.3. Methodology for Ramp Irradiance Classification Using Irradiance-Based Extreme Day Identification Method

Considering the limitations encountered in classifying ramp classes when using the described method based on standard deviation scoring, it was concluded that a methodology for assigning class boundaries for irradiance should be developed. As a result, the following methodology was proposed which includes in steps 6 to 9 the method based on standard deviation score, but adds new mechanisms to tackle the task of finding class boundaries for any irradiance dataset.

The methodology relies on including a method capable of responding to the weaknesses outlined in the previous section, the Irradiance-Based Extreme Day Identification (IBEDI) method (Algorithm 2). The most important condition that the method fulfils is that of creating class boundaries from the data of the specific problem. This condition would facilitate its generalization, decoupling the application of the method from fixed predefined bounds.

Algorithm 2. Methodology for ramp irradiance classification using IBEDI method

1. Data Collection and Preprocessing:
2. Collect solar irradiance data.
3. Verify and clean data to remove outliers or incomplete data that may affect the accuracy of the analysis.
4. Compute extraterrestrial irradiance and clearness index data by location.
5. Visualization and Exploratory Analysis:
    - Generate plots of all days in the dataset to visualize temporal variability of solar irradiance (To be employed in small datasets).
6. Calculate the ramps
7. Quantify the ascending and descending ramps.
8. For ascending ramps calculate:
    - Average
    - Standard deviation
    - Standard deviation score
9. For downward ramps calculate:
    - Average
    - Standard deviation
    - Standard deviation score
10. Calculate the class boundaries based on the evaluated data:
    - Classify days whether they are clear, partially cloudy, or cloudy.
    - Identify extremely clear and cloudy days.
    - Execute the agglomerative algorithm for the days selected in the previous step.
    - Obtain class limits.
11. Rank the ramps according to the limits set in the previous step for the absolute value of the standard deviation score.

The Algorithm 2 begins with data collection and preprocessing, which involves gathering solar irradiance time series and verifying it to ensure accuracy by removing outliers and incomplete entries. Extraterrestrial irradiance and clearness index data are then computed based on the specific location. Following this, visualization and exploratory analysis are conducted by generating plots to illustrate the temporal variability of solar irradiance, particularly useful for smaller datasets.

For the analysis, solar irradiance ramps are first calculated. Then, both upward and downward ramps are quantified. For both upward and downward ramps, the average, standard deviation and standard deviation score are calculated, following the same statistical evaluation process in both directions.

We split the irradiance time series in days and then classify them as clear, partially cloudy, or cloudy based on the clearness index, using established measurement limits from previous irradiance studies for automated classification. Three groups are created, one for each classification.

To identify the most representative days within each group, a method is employed to automatically select extremely clear and cloudy days. This method uses the Root Mean Square Deviation (RMSD) to measure the difference between global irradiance and extraterrestrial irradiance. Finally, the selection is refined to ensure that the chosen days accurately represent both typical and extreme solar irradiance conditions.

The agglomerative clustering algorithm is used to determine class boundaries. As input to the agglomerative, we use the Z value of the extreme days selected in the previous step. Values are already scaled. As a final step, we classify the ramps using the Z score values and the limits found with the agglomerative. Our approach aims to be scalable, accommodating datasets of varying sizes. The next section explains this algorithm in the context of the IBEDI method.

2.3.1. Agglomerative Clustering Algorithm

A method of unsupervised machine learning is used to implement the proposal raised in the previous section. In particular, clustering is employed because of the advantage of creating groups without prior knowledge of the data to be grouped. Within the clustering methods, there are different types: density-based, distance-based, distribution-based, centroid-based, or hierarchy-based methods.

The hierarchy-based algorithm organizes the data points in a tree structure (hierarchy) and follows a bottom-up process of grouping based on the similarity between the data points. In particular, we use the agglomerative clustering consisting of splitting the dataset into individual nodes and merging the current pair of nodes closest to each other step by step into a new node until there is a final node comprising the entire dataset [12], which is constructed in the form of a dendrogram as shown in Figure 2. To create the clusters, a level of the dendrogram is selected and pruned; depending on the level chosen, the clusters can be more or less compact.

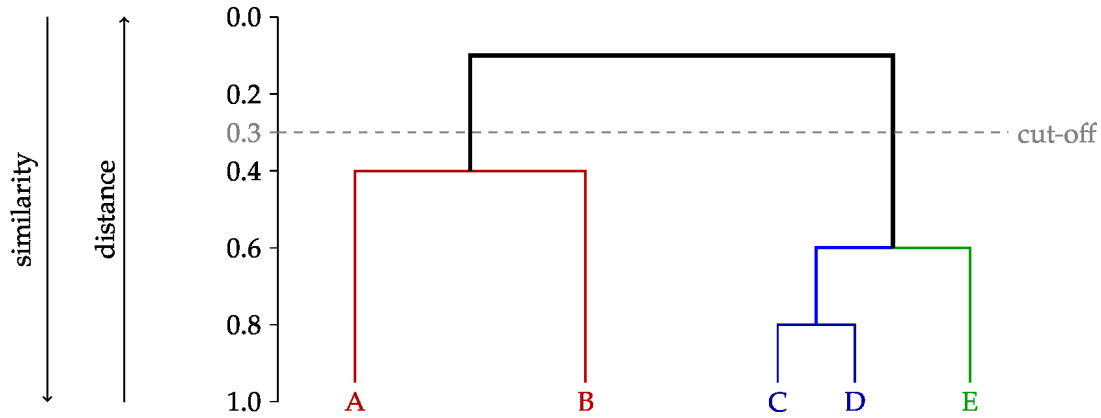

Figure 2. Representation of a generic dendrogram. Categories and values in the axis are only included as an example. Note: The letters A-E represent the elements to be grouped.

The agglomerative algorithm is an option to consider for clustering for several key reasons. First, it is simple and efficient to apply, as it starts with each data point as an individual cluster and progressively merges the closest clusters. This makes it intuitive and easy to apply. Secondly, it adapts well to data with different cluster shapes and sizes, which is useful when the data do not follow a uniform distribution. In addition, the agglomerative approach offers flexibility in the choice of distance metrics, allowing it to adapt to different types of data, including numerical, categorical, or mixed data. Finally, unlike other methods, agglomerative clustering does not require random initialization, which ensures consistent results without the risk of poor starting points affecting the final result.

To choose the best configuration of parameters for the agglomerative algorithm, experiments were carried out with each of the configurations and evaluated with the silhouette score, using a combination of metrics and linkages. For the metrics parameter, the following values were tested: “Euclidean” and “Manhattan”. Euclidean and Manhattan distances offer distinct approaches for quantifying the separation between data points in a space.

Euclidean distance computes the shortest path or direct line between two points, capturing the geometric distance as a straight line. In contrast, Manhattan distance calculates the cumulative distance by summing up the absolute differences along each axis. For the linkage parameter, the following values were tested: "ward", "complete", "average", and "single". The "ward" method minimizes the variance within clusters as they are merged, while the "average" method calculates the mean distance between each observation in the two sets. The "complete" linkage approach uses the maximum distance between all observations of the two sets, whereas the "single" linkage method relies on the minimum distance between observations from each set.

The silhouette score is a metric used to assess the quality of clustering results. It measures how well each data point is clustered by considering both the cohesion and separation of clusters. Cohesion evaluates how similar a point is to other points within the same cluster, calculated as the average distance between the point and all other points in the same cluster. Separation measures how similar the point is to points in the nearest cluster that is not its own, calculated as the average distance to all points in the nearest neighboring cluster. The silhouette score for a data point is given by Equation (5):

$$s(i) = \frac{b(i) - a(i)}{\max(a(i), b(i))} \tag{5}$$

where $a(i)$ is the cohesion, the average distance to points in the same cluster, and $b(i)$ is the separation, the average distance to points in the nearest cluster. The score ranges from -1 to 1. Values close to 1 indicate that the point is well clustered, meaning it is closer to points in its own cluster than to points in other clusters. Values close to 0 suggest that the point is on the boundary between clusters, showing that it is roughly equidistant from clusters. Negative values indicate that the point might be misclassified, as it is closer to a different cluster than its own. The average silhouette score across all points provides an overall measure of clustering quality.

2.3.2. Classified and Cluster Days Based on Clearness Index

Days can be classified as clear, partially cloudy, or cloudy based on the daily clearness index (K_{td}), the ratio between global horizontal irradiance, and the irradiance at the top of the atmosphere (Equation (6)).

$$K_{td} = \frac{GHI_d}{I_{0d}} \tag{6}$$

In their literature review, Reno and Hansen [13] highlight how different clearness index limits have been used to obtain clear and cloudy days. Values above 0.6 or 0.65 or 0.7 have been taken as clear days in different studies. Other studies used four intervals for classification: cloudy sky, partially cloudy sky, partially clear sky, and clear [14,15]. In this study, we use only three classifications (clear, partially cloudy, or cloudy) and a threshold of 0.65 as presented in [16] for clear days. The imprecision may arise from choosing different values for this threshold arising because K_{td} is not a pure function of cloudiness [17]; therefore, this was considered in the next step of the methodology, where most extreme days were selected from these a priori formed groups.

The classification used for IBEDI is defined as follows:

- Clear days: Days with a K_{td} value ranging between 0.65 and 1.0 are considered clear. These days typically exhibit minimal cloud cover, allowing for a high proportion of solar radiation to reach the Earth's surface.
- Partially cloudy days: Days with a K_{td} value ranging from 0.3 to 0.65 fall into the partially cloudy category. On these days, intermittent cloud cover causes signifi-

cant fluctuations in the amount of solar radiation received, resulting in moderate irradiance levels.

- Cloudy days: Days with a K_{td} value between 0 and 0.3 are classified as cloudy. These days are characterized by extensive cloud cover, which significantly reduces the amount of solar radiation that reaches the surface, leading to lower irradiance values.

For the classification of days, the daily K_{td} was calculated with Equation (6), where GHI_d is the daily average of global irradiance on the horizontal plane and I_{0d} is the daily average of top-of-atmosphere irradiance on the horizontal surface and has been calculated using "Solar Geometry 2" library [18].

Figure 3 shows the distribution of clear, partly cloudy, and cloudy days obtained using the clearness index.

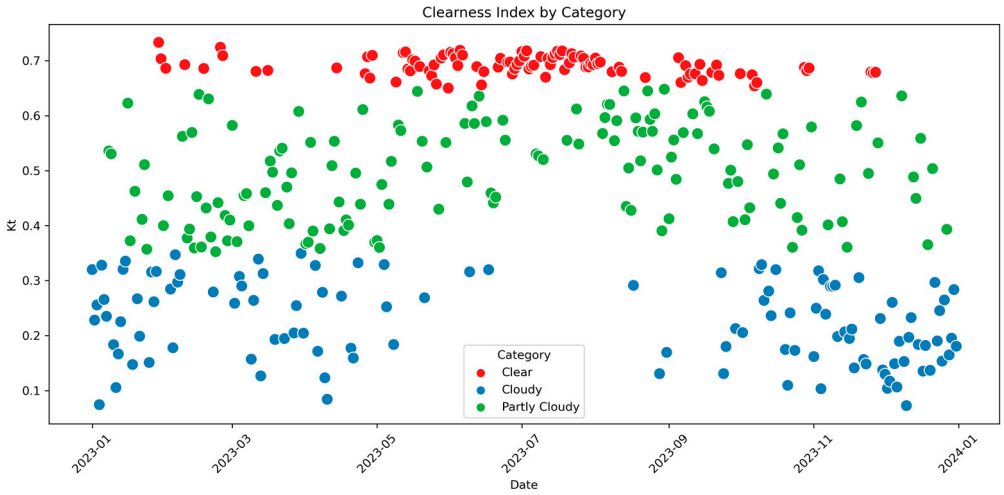

Figure 3. Clearness index values differentiating the categories by color. Red color represents clear days, green color represents partly cloudy days, and blue color represents cloudy days.

2.3.3. Identification of Extremely Clear and Cloudy Days

The RMSD metric (Equation (7)) is used to identify extreme days, classified as either clear or cloudy. This metric compares the irradiance measured at the Earth's surface with the extra-atmospheric irradiance (theoretical in the absence of atmosphere). RMSD is used here as a "distance" metric similar to the Euclidean, measuring the deviation between observed and theoretical values. The larger this distance, the more extreme the daytime condition (whether clear or cloudy) is considered, facilitating accurate identification, which can be expressed with the following equation:

$$RMSD = \sqrt{\frac{1}{n}\sum_{i=1}^{n}(\mathrm{GHI} - I_0)^2} \tag{7}$$

3. Data

This section provides a detailed description of the datasets analyzed in the study, along with an outline of the key preprocessing steps applied to each dataset.

3.1. Datasets

3.1.1. Portugal Dataset

The first dataset used in this research is from a photovoltaic power station previously described and analyzed in [19,20]. The station data include global irradiance in the horizontal plane measured by a pyranometer, global irradiance in the generator plane measured by a calibrated cell, and wind speed. The data were measured with a time resolution of

5 s. A total of 168 complete days are available from 2010 to 2013. The year 2012 is the least represented with 4 days and the year 2013 is the most represented with 143 days.

3.1.2. Oregon Dataset

The second dataset is from the Solar Radiation Monitoring Laboratory (SRML) at the University of Oregon [21]. It is public and provided by the National Renewable Energy Laboratory (NREL). The SRML is a network of high-quality and low-quality stations. High-quality stations measure all irradiance components, at a 1 min resolution. The Global CMP22 and LI-200R pyranometers measure global irradiance, direct, and diffuse radiation. Low-quality stations measure at an hourly frequency. The dataset also includes other meteorological variables. It is updated daily and has been available since August 2016. For the study to be carried out, raw data for the year 2023 was downloaded.

3.1.3. Hawaii Dataset

The third dataset used in this study is a public dataset and was selected from the NREL [22]. It has 17 irradiance sensors on Oahu Island, Hawaii in approximately one square kilometer. The time resolution is 1 s global horizontal irradiance (GHI) measured in the period (March 2010 through October 2011).

3.2. Preproccesing Data

In addition, a selection of variables was made, working only with the pyranometer data, leaving the inverter data for future work.

The astronomical variables (irradiance at the top of atmosphere, extra-atmospheric irradiance, and solar elevation angle) required for the irradiance analysis were retrieved from the "Solar Geometry 2" library [18] for the three datasets. The GHI values for the three datasets were taken for solar elevation angles greater than 2° [23].

During the initial data analysis for Hawaii data, information related to the AP3 sensor was excluded due to missing data, resulting in a dataset comprising information from 16 sensors. As part of the data pre-processing, the dataset was resampled at 10 s intervals [24].

After the preprocessing for each dataset, we have two variables to use as input of the methodology: GHI and irradiance at the top of atmosphere. For the Portugal dataset, we have 168 days with a resolution of 5 s. In the case of the Hawaii dataset, we will use the GHI from the DH3 station with 600 days and a resolution of 10 s. The Oregon dataset has 365 days of GHI with a resolution of one minute. As a threshold to calculate the ramps, we will use the temporal granularity of each dataset.

4. Results

This section presents the results of the application of the proposed methodology. We start with the search for the best parameters for the agglomerative algorithm. Then, we cluster all the days present in the dataset based on the clearness index. To find the representative days, the next step was to find the significant days to be used with the agglomerative algorithm with the IBEDI method. After applying the method, the minimum amount of data needed to find the class boundaries with the agglomerative clustering algorithm is calculated. The limits found are applied and the irradiance ramps are classified. The results are described for each of the datasets analyzed with the methodology.

4.1. Comparison of Different Configurations of the Agglomerative Clustering Algorithm

The silhouette score was used to compare different configurations of the agglomerative algorithm. Table 1 shows the results. The ward linkage method was only tested with the Euclidean distance because it has the condition that it excludes the use of ward with any

metric other than Euclidean, since ward is only compatible with the Euclidean metric. This configuration has the lowest silhouette score with 0.94 and the combinations with average and single for both Euclidean and Manhattan are the best with 0.97.

Table 1. Silhouette scores for different linkage methods and distance metrics for the agglomerative algorithm.

Linkages	Metric	
	Euclidean	**Manhattan**
ward	0.94	-
complete	0.96	0.96
average	0.97	0.97
single	0.97	0.97

In this particular problem, we have selected the configuration that combines the Euclidean distance with the linkage average method. This study implemented the Scikit-learn library [25]. The creation of four groups was used as a stopping mechanism for the algorithm, so that the number of groups would coincide with the method based on standard deviation score. The classes followed the same naming pattern: low, moderate, high, and severe.

4.2. Cluster Days Based on Clearness Index

Figure 4 presents a sample of the result of the clustering by clearness index method for the complete Oregon dataset. It is shown with three subplots. The subplot on the left represents a clear day and the RMSD in a per-unit scale data was recorded on 3 June 2023. The time series is plotted in blue and shows a pattern characteristic of a clear day, with steady increases and decreases in irradiance throughout the day. The center subplot represents a partially cloudy day, the RMSD in a per-unit scale data was recorded on 14 August 2023. On the other hand, the right subplot represents a cloudy day, the RMSD in a per-unit scale data was recorded for 25 September 2023. Subplots (b) and (c) show a ramp pattern, indicative of fluctuating cloudiness throughout the day.

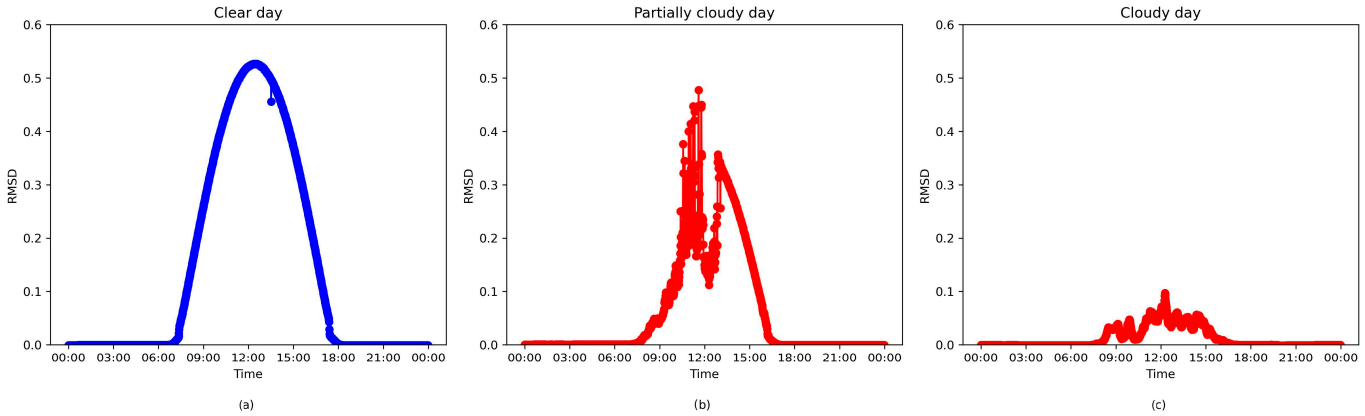

Figure 4. Sample of days classified using the clearness index for the Oregon dataset. The left subplot represents a clear day (**a**) GHI data recorded on 3 June 2023. The center subplot represents a partially cloudy day, (**b**) GHI data recorded on 14 August 2023. The right subplot represents a cloudy day, (**c**) GHI data for 25 September 2023.

4.3. Identifying Extreme Days

Figure 5 presents the result of the IBEDI method for the identification of extreme days. The figure represents two specific days in January; from the Oregon dataset, each represent

different weather conditions. The left subplot displays a clear day, data measurements were recorded on 16 January 2023. The day was characterized by clear sky conditions with RMSD in a per-unit scale value of 0.07, reflected in the consistent pattern. The right subplot represents a cloudy day, data were recorded for 1 January 2023. This plot shows more variability with RMSD in a per-unit scale value of 0.16, indicative of cloudy weather conditions.

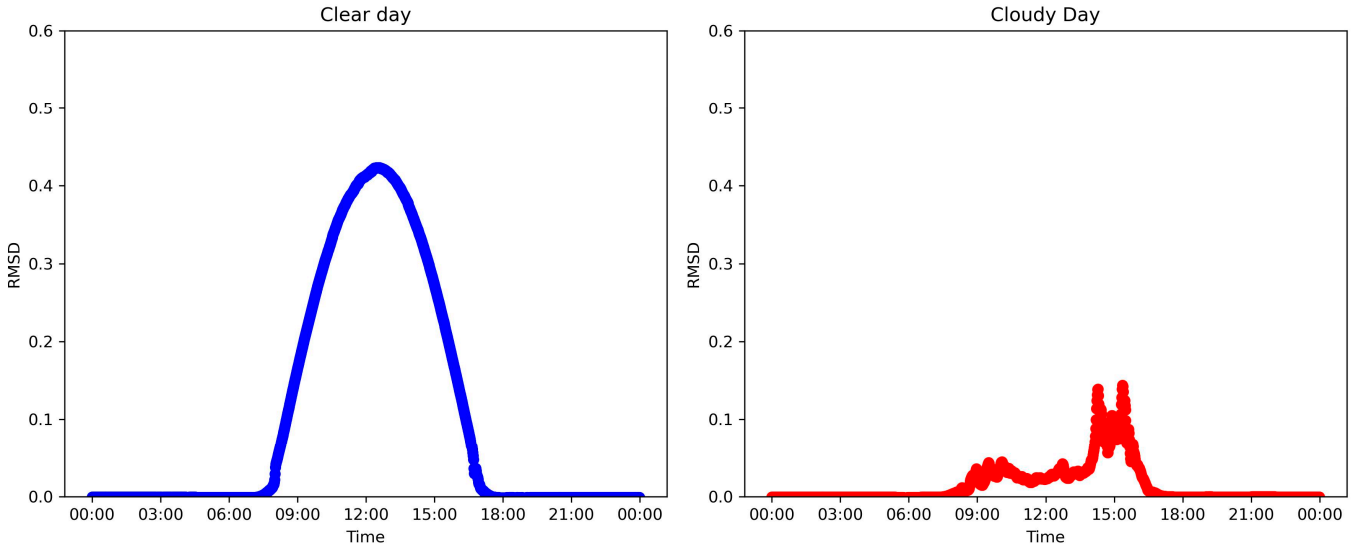

Figure 5. Selection based on the identification of extremely clear and cloudy days. The left subplot represents a clear day, GHI data recorded on 29 January 2023. The right subplot represents a cloudy day, GHI data for 18 January 2023.

We consider that the IBEDI method for the identification of extremely clear and cloudy days has good results because it obtains well-differentiated days. This is important to obtain groups of classes with an adequate distance because the agglomerative algorithm relies on distance to create the groups. These distances are clearly marked in cloudy days with more variability and clear days with a smoother curve.

4.4. Results of Ramp Clasification for Portugal Dataset

For this particular dataset, only the first two steps of the methodology are used because it is possible to determine which days had more or less variability by visual inspection of the plots for each of the days. This is due to the small size of the dataset. After selecting the most representative days, we start with one day and gradually increase it until no substantial changes are observed in the class limits reached. In this particular time, the limit of days used remains at ten. It is important to note that the temporal resolution of the data is 5 s, so only one day has 12,961 irradiance records from 3 a.m. to 9 p.m. Because of this, with ten days, the algorithm has enough elements to consider. In addition, the evaluation of the quality of the algorithm's output can be reinforced by visual inspection of the achieved classes.

Figure 6 shows the differences between the relative frequencies found between one day and ten days with the agglomerative algorithm. The image on the left shows that, with increasing data, the algorithm defined clearer boundaries between high and moderate classes, as opposed to one day of data (image on the right Figure 6).

By applying the modified algorithm to this particular problem, we have found that the low class includes values below 0.62, the moderate class includes values between 0.62 and 3.51, the high class includes values between 3.51 and 6, and the severe class includes

values greater than 6. Figures 7 and 8 show the result of applying the proposed algorithms for days with and without clouds.

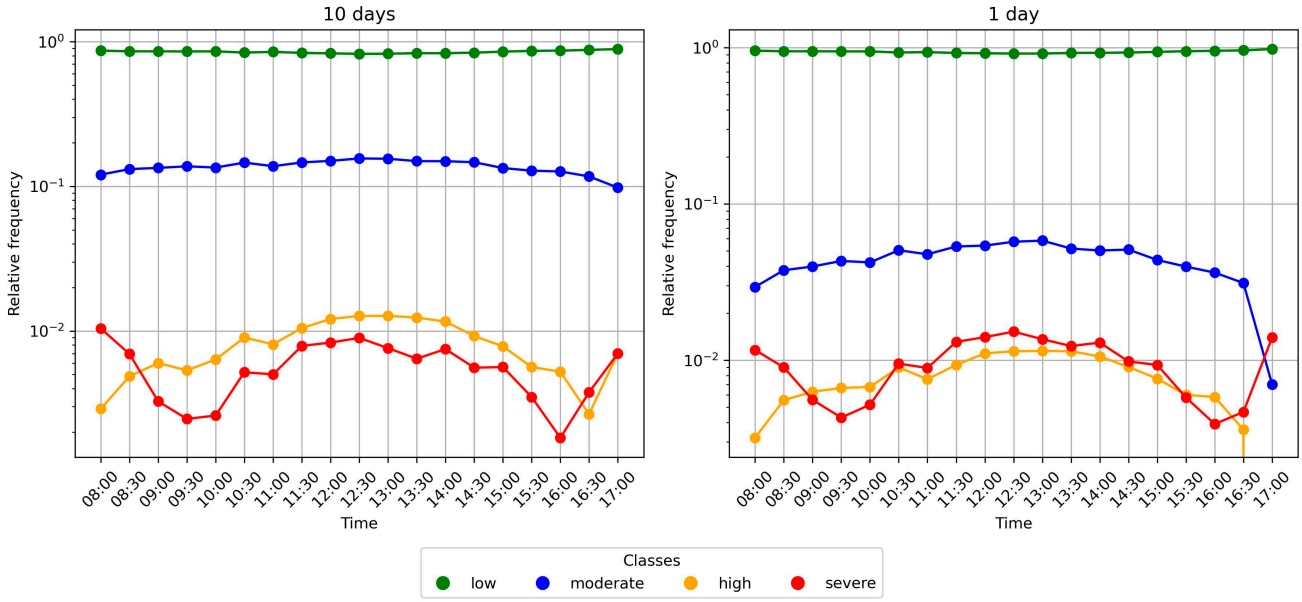

Figure 6. Relative frequency using a logarithmic scale, 10-day records on the left to train the agglomerative algorithm and on the right using one day.

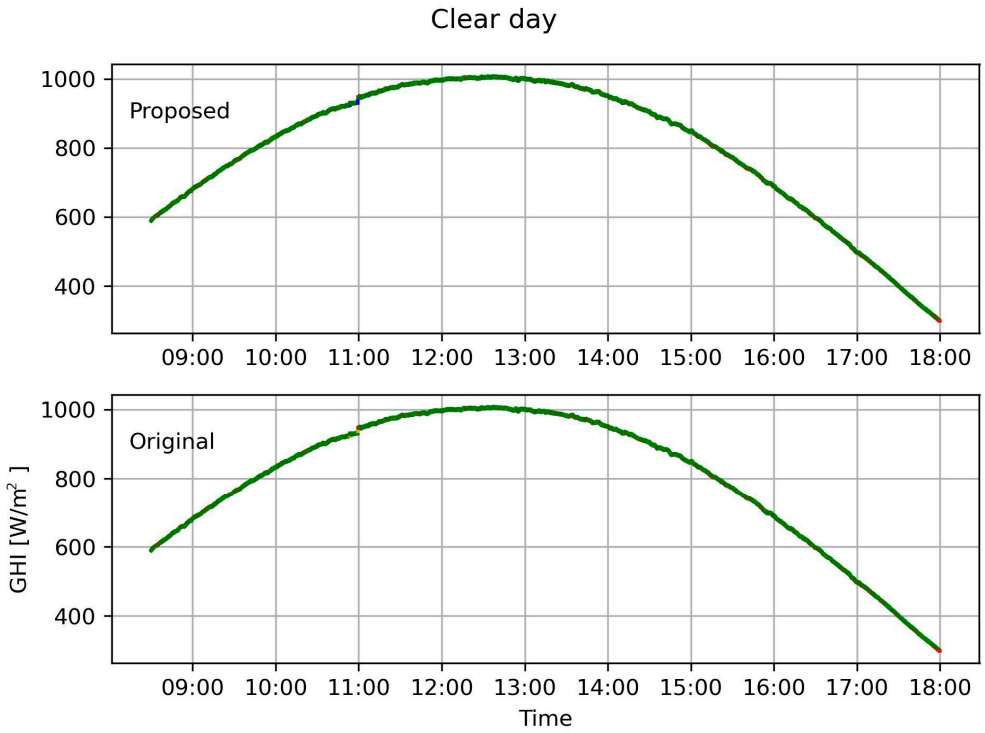

Figure 7. Result of the application of the algorithms—original and proposed—on a clear day. Note: Original refers to method based on standard deviation score and proposed refers to the methodology based on IBEDI method. Green represents the low class.

In an ideal environment with clear sky (Figure 7), both algorithms demonstrate the ability to classify global irradiance without drawbacks. Under cloudy sky conditions, it is observed that while the method based on standard deviation score classifies only three classes, the proposed algorithm is able to classify four (Figure 8). Although the results indicate that the classification is more accurate with the newly identified boundaries, it

is crucial to further investigate the classification and its correspondence to the reality of a power grid.

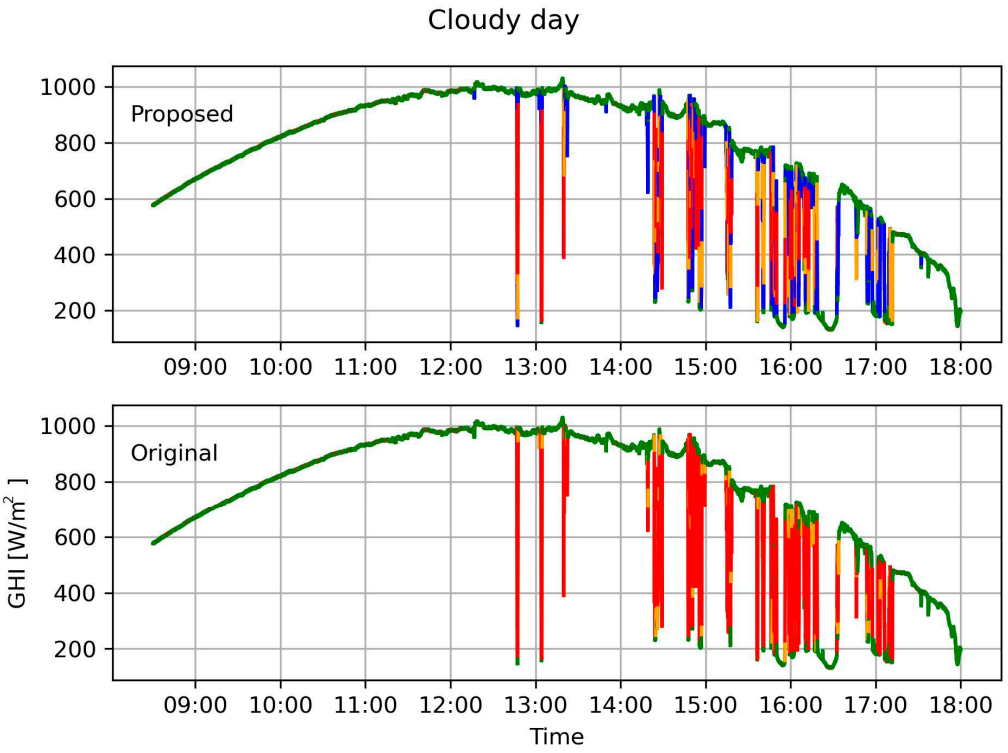

Figure 8. Result of the application of the algorithms—original and proposed—on a cloudy day. Note: Original refers to method based on standard deviation score and proposed refers to the methodology based on IBEDI method. Green represents the low class, blue the moderate class, orange the high class, and red the severe class.

Table 2 summarizes the relative frequency by class for each year. The low class is the most frequent for all years, followed by the severe class. The moderate and high classes, although also present, have a low frequency compared to the other two classes. The high class is the least frequent.

Table 2. Relative frequency by class and by year of the modified algorithm for Portugal dataset.

Year	Low	Moderate	High	Severe
2010	0.74	0.058	0.007	0.189
2011	0.73	0.037	0.006	0.224
2012	0.69	0.103	0.008	0.200
2013	0.58	0.137	0.006	0.271
Average	0.68	0.080	0.007	0.221

Figure 9 shows the results of the relative frequency analyzed for the year 2013, considering the interval from 0600 in the morning to 1800 in the evening. It can be seen that the method based on standard deviation score leaves one class empty (left of Figure 9), while the proposed modification includes all four classes (right of Figure 9).

4.5. Results of Ramp Clasification for Oregon Dataset

For this dataset, we use a method based on irradiance comparison for the identification of extremely clear and cloudy days to determine the most representative days. In order to ensure that the sample of classes had the best possible representation in terms of the seasons of the year, after grouping all the days in the dataset according to whether they were clear,

partly cloudy, or cloudy, the method was applied. As a result of this selection, 10 days were used for the input to the agglomerative model. This yielded the following limits for the four classes tested. The "Low" class includes values under 0.23, the "moderate" class covers values from 0.23 to 0.55, the "High" class spans from 0.55 to 1.18, and the "Severe" class comprises values above 1.18.

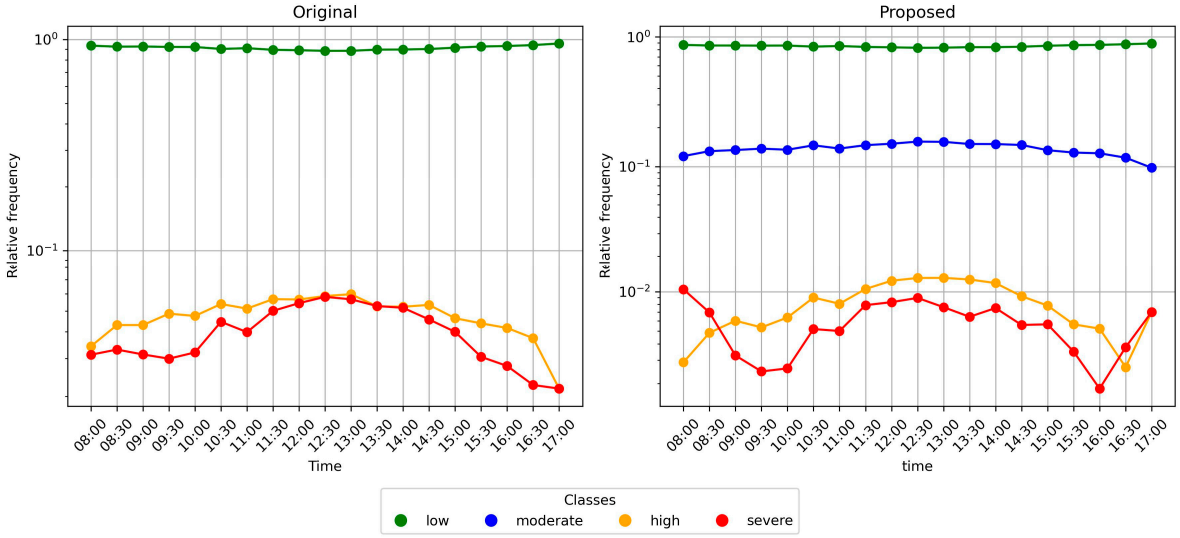

Figure 9. Relative frequency using a logarithmic scale, grouped by time of day for the classes found for the year 2013 in Portugal dataset. On the left results of the original algorithm and on the right results of the modified algorithm. Note: Original refers to method based on standard deviation score and proposed refers to the methodology based on IBEDI method.

Figure 10 presents the results of the relative frequency analysis for the period from January to December 2023, based on Oregon data. The analysis considers the interval from 0800 in the morning to 1700 in the evening and includes all four ramp classes. During the central hours of the day, the "low" and "moderate" classes are the most prevalent. In contrast, "severe" and "high" classes while present exhibit the lowest overall frequency.

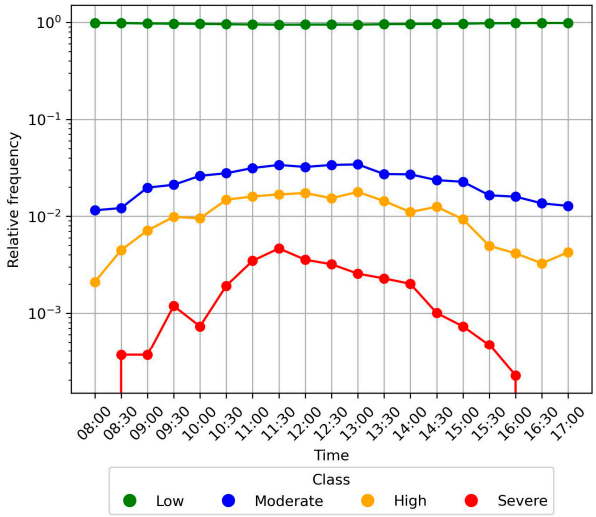

Figure 10. Relative frequency using a logarithmic scale, grouped by time of day for the classes found in Oregon dataset for 2023 data.

Table 3 presents the relative frequency of ramps categorized as low, moderate, high, and severe across the months of 2023 in Oregon. On average, the most prevalent class is "low", with a frequency of 0.91 (91%), while the "moderate" class is less common, appearing

with an average frequency of 0.07 (7%). The "high" and "severe" classes are rare, with mean frequencies of 0.01 (1%) each, being more frequent during spring and autumn. In the winter and summer months, the frequency of "low" conditions is highest (between 0.95 and 0.97), while "severe" conditions only occur in low proportions during spring and autumn, reflecting a seasonal distribution of higher intensities.

Table 3. Relative frequency for the year 2023, data from Oregon.

Month	Low	Moderate	High	Severe
January	0.95	0.04	0	0
February	0.9	0.08	0.01	0
March	0.87	0.1	0.02	0.01
April	0.82	0.13	0.03	0.02
May	0.87	0.08	0.02	0.03
June	0.91	0.07	0.01	0.01
July	0.97	0.02	0.01	0
August	0.95	0.04	0.01	0.01
September	0.88	0.09	0.02	0.01
October	0.91	0.07	0.01	0.01
November	0.95	0.05	0	0
December	0.97	0.03	0	0
Average	0.91	0.07	0.01	0.01

4.6. Results of Ramp Clasification for Hawaii Dataset

When applying the methodology to select the representative days in this dataset. the resulting days for each of the sensors were practically the same except for sensor DH2 which varied by two months and sensors DH7 and DH1 which varied by one month. Because of this. it was decided to work only with the data from sensor DH3. Through the application of the proposed algorithm to this specific problem, we identified that the "low" class encompasses values below 1.078, the "moderate" class ranges from 1.078 to 3.54, the "High" class covers values between 3.54 and 7.158, and the "severe" class includes values exceeding 7.158.

Figure 11 shows the results of the relative frequency analyzed for the period from April 2010 to March 2011 for DH3 sensor data. Considering the interval from 0600 in the morning to 1700 in the evening, it can be seen that the figure includes all four classes. In the central hours of the day, the moderate, high, and severe classes are the most frequent. On the contrary, in the hours of sunrise and sunset, the most frequent classes are low and moderate. The severe class has the lowest frequency.

The data provided in Table 4 reflects the relative frequency of classes found (low, moderate, high, severe) from April 2010 to March 2011 in Hawaii. The "low" class consistently dominates with values ranging from 0.69 to 0.863, indicating that the majority of cases or events fall into this category throughout the year. Notably, the months of January and February exhibit the highest relative frequencies in the "low" class, suggesting a significant prevalence of low-intensity occurrences during these months. Conversely, the "moderate" and "high" classes show much lower frequencies across all months, indicating that moderate to high occurrences are less common. In contrast, the "severe" class demonstrates a noticeable increase as the year progresses, particularly from August to December, where the frequency rises from 0.169 to 0.279, the highest observed value for the period. This trend suggests a seasonal pattern where severe cases or events are more frequent towards the end of the year. The average values for the year further emphasize this distribution with the "low" class maintaining the highest average (0.779) and the "severe" class following as

the second most frequent (0.174), highlighting a distinct pattern of severity intensifying towards the latter months of the year.

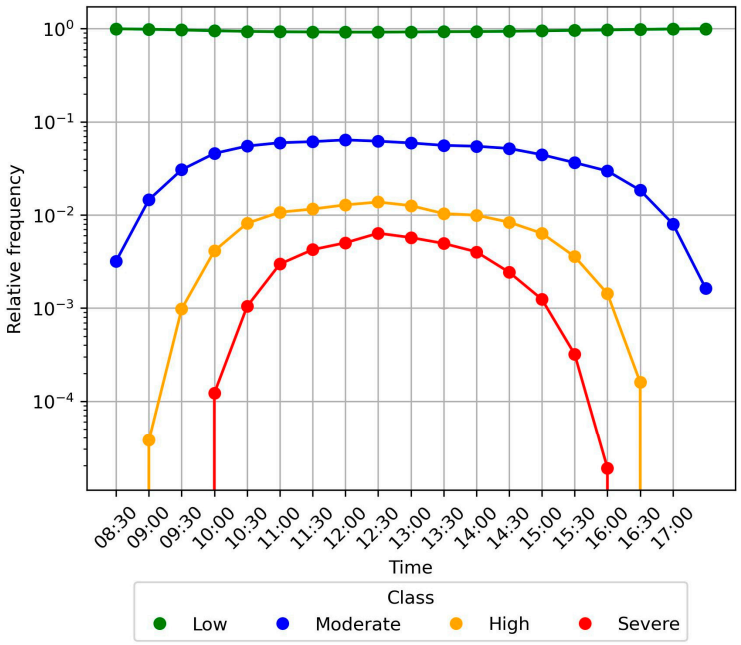

Figure 11. Relative frequency using a logarithmic scale, grouped by time of day for the classes found for the period of April 2010 to March 2011 in Hawaii dataset for DH3 sensor data.

Table 4. Relative frequency by month from April 2010 to March 2011 data from Hawaii dataset.

Month	Low	Moderate	High	Severe
April	0.794	0.04	0.015	0.151
May	0.801	0.044	0.018	0.138
June	0.8	0.053	0.022	0.125
July	0.794	0.049	0.02	0.137
August	0.762	0.048	0.021	0.169
September	0.752	0.038	0.016	0.194
October	0.721	0.031	0.01	0.238
November	0.69	0.023	0.007	0.279
December	0.716	0.01	0.002	0.273
January	0.845	0.018	0.005	0.132
February	0.863	0.017	0.003	0.117
March	0.813	0.039	0.016	0.132
Average	0.779	0.034	0.013	0.174

5. Discussion

5.1. Impact of Proposed Methodology

Sections 4.4–4.6 present the results of applying the methodology proposed in Section 2.3 to the datasets studied. For each dataset, different class boundaries were obtained after applying the proposed method. For this study, 10 days were used as input to the agglomerative for all datasets.

Table 5 presents the class boundaries for the absolute value of Z score across three datasets: Portugal, Oregon, and Hawaii. Each row represents a class (low, moderate, high, severe), showing the specific Z score range for each dataset. This layout allows for a quick comparison, highlighting how each location has distinct thresholds to define the ramp within each class. Figures 12 and 13 show the ramp classifications represented for one day

from the Oregon and Hawaii datasets. On both days, the four classes are found, although for their classification, the limits used were different.

Table 5. Class boundaries determined after application of the proposed methodology.

Class	Dataset		
	Portugal	**Oregon**	**Hawaii**
Low	$Z < 0.62$	$Z < 2.17$	$Z < 2.19$
Moderate	$0.62 \leq Z \leq 3.51$	$2.17 \leq Z \leq 5.01$	$2.19 \leq Z \leq 5.88$
High	$3.51 < Z \leq 6$	$5.01 < Z \leq 10.72$	$5.88 < Z \leq 8.01$
Severe	$Z > 6$	$Z > 10.72$	$Z > 8.01$

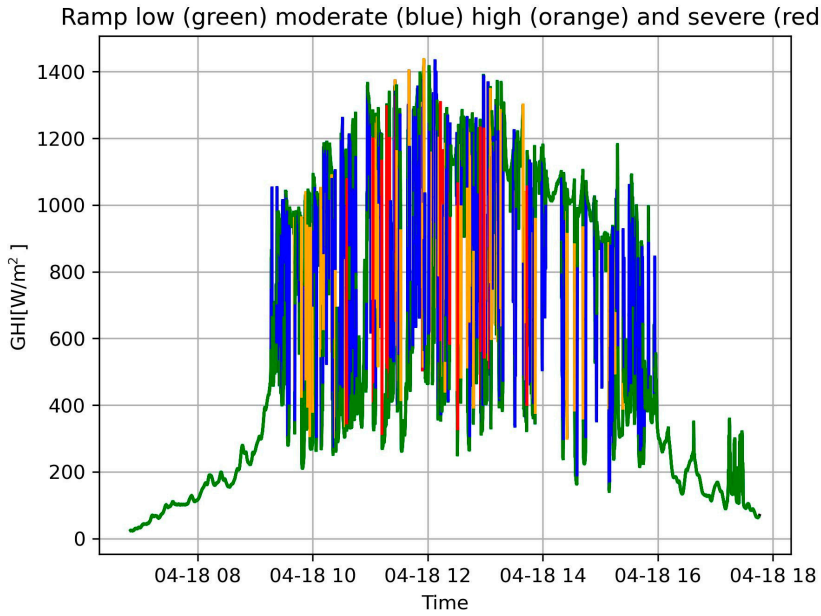

Figure 12. Classes obtained from the irradiance ramps after applying the proposed methodology to one day of data from DH3station in Hawaii dataset. Note: Green color represents the low class, blue color the moderate class, orange color the high class, and red color the severe class.

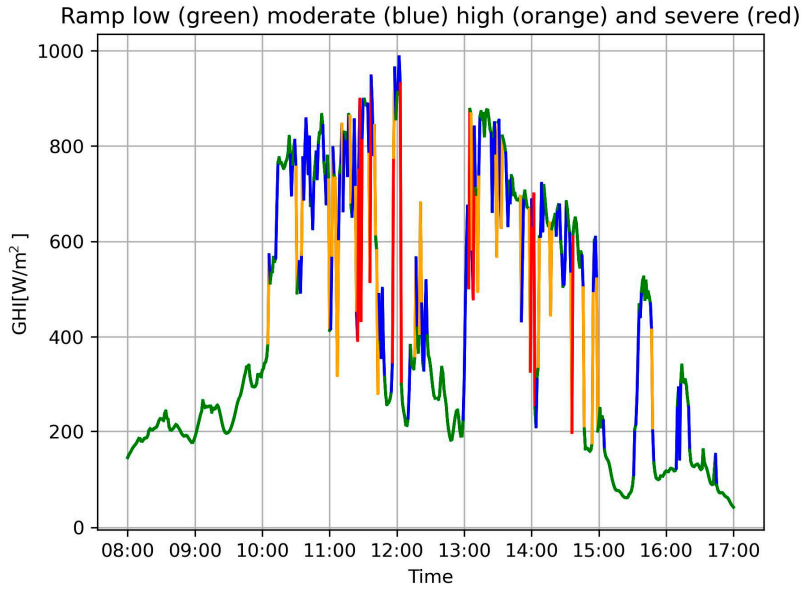

Figure 13. Classes obtained from the irradiance ramps after applying the proposed methodology to one day of data from the Oregon dataset. Note: Green color represents the low class, blue color the moderate class, orange color the high class, and red color the severe class.

Different datasets of different temporal resolutions and from different geographic locations have been worked with, and for each of them, the limits found with the proposed methodology have been different. It is therefore to be expected that for a new dataset, the limits will be new. The limits depend directly on the selected extreme days, and the classification of the days is a function of the climate of the region.

The relative frequency of the severe class in the Portugal and Hawaii datasets is high compared to the Oregon dataset which is almost zero. In the first two datasets, the temporal resolution is seconds while the other dataset has a resolution of one minute; this influences the classification of the ramps because the ramp depends directly on the Δt used to calculate it initially [26]. Moreover, the number of ramps to be classified in these datasets is higher. However, for the moderate and high classes, the relative frequency maintains a similar behavior in the three datasets. The low class has a lower relative frequency in the Hawaiian and Portuguese datasets compared to the one found in the Oregon dataset. The severe class shows expected behavior when compared to the lower class.

The proposed IBEDI method allows for the generalization of the irradiance ramp classification to any irradiance dataset, because the method establishes the means to calculate the limits specific to each dataset in question.

5.2. Solar Irradiance Variability and the Impact of Photovoltaic Systems on Electrical Grids

The variability of solar irradiance is the cause of fluctuations in the power produced by photovoltaic systems. Several studies have analyzed the performance of photovoltaic systems from this perspective, observing that the variability present in solar irradiance is attenuated both by the spatial dispersion among systems and within a photovoltaic system itself [27,28].

On the one hand, it can be stated that the spatial dispersion of different photovoltaic systems connected to the same grid attenuates the combined variability. The level of attenuation primarily depends on the meteorological characteristics of the area and season, and the distance between the systems [26,29–31].

On the other hand, the attenuation of variability also occurs within photovoltaic systems [19,32,33]. The analysis of the time series of power delivered by a set of DC/AC inverters belonging to the same large-scale plant is consistent with the description of a photovoltaic system as a low-pass filter: high frequencies are attenuated because there is no correlation between the different time series; low frequencies remain unchanged because the correlation reaches values close to unity; and the attenuation of intermediate frequencies depends on the distance between the inverters and on the daily fluctuation level.

Nevertheless, because maintaining an instantaneous balance between generated and consumed power is crucial for electrical grid operation, the combined variability of multiple photovoltaic systems can have a significant impact. This impact has resulted in the formulation of regulations and recommendations for photovoltaic system integration.

To quantify this impact, an analysis of the interaction between the electrical grid, consumption elements, and photovoltaic systems is required. This analysis is conducted through the development of comprehensive models that incorporate variations across these three domains. These models account for intrinsic component characteristics (e.g., PV system power output, consumption node demand), temporal variability (e.g., industrial and domestic consumption profiles, radiation models), and spatial factors (e.g., inter-system and node distances, diverse climatological conditions at generation sites).

An illustrative example of this analytical approach is presented by Uruel and Perpiñan [34], who performed a steady-state power-flow analysis on multiple electrical distribution networks integrating consumption nodes and distributed photovoltaic generation. Their model considers wire characteristics, electrical network topology layout, hourly en-

ergy consumption profiles, and hourly PV-system generation profiles. However, assessing the impact of variability requires consideration of shorter time scales and thus an analysis of the network's transient behavior. A detailed investigation of this transient-state power-flow analysis is outside the scope of our work and is reserved for future study.

6. Conclusions

In this study, a new methodology for an irradiance classification ramp have been proposed. A ramp classification method found in the literature has been used, improving the proposal with methods generalizable to any irradiance dataset. The used method stated that although the standard deviation-based score ranking technique was presented for wind data, it was generalizable to solar data.

The methodology covers the series of steps necessary to find class boundaries based on the data and the specific problem. To do this, it was proposed to use an agglomerative clustering method on a subset of the data. This would calculate the class boundaries to be used using the absolute value of the score proposed in the method based on standard deviation score.

The main contribution is that, by establishing a new method for finding the class boundaries, the classes are better matched to the classification. Furthermore, the observations made to the method based on standard deviation score are resolved, since no class is empty. For this purpose, the methodology has grouped the days of the dataset according to whether they are clear, partially cloudy, or cloudy and this groups are used to find representative days to be used like input in the agglomerative algorithm. The proposed method identifies the extreme days using the RMSD metric between global irradiance and extraterrestrial irradiance.

Three datasets from distinct geographic regions—Oregon (northwestern United States), Hawaii (central Pacific Ocean), and Portugal (southwestern Europe)—each with varying temporal resolutions of five seconds, ten seconds, and one minute—were analyzed.

The class boundaries for each dataset resulted in different limits compared to those produced by the method based on standard deviation score. With the new limits, representation was found in all four classes for all datasets.

Future research will address the translation of this classification to photovoltaic systems interconnected with electrical grids, evaluating the impact of each of them on the stability of the network.

Author Contributions: Conceptualization. L.B.C. and O.P.-L.; methodology. L.B.C. and O.P.-L.; software. L.B.C.; validation. L.B.C. and O.P.-L.; formal analysis. L.B.C.; investigation. L.B.C.; resources. O.P.-L.; data curation. L.B.C. and O.P.-L.; writing—original draft preparation. L.B.C.; writing—review and editing. L.B.C. and O.P.-L.; visualization. L.B.C.; supervision. O.P.-L.; project administration. O.P.-L.; funding acquisition. O.P.-L. All authors have read and agreed to the published version of the manuscript.

Funding: This research and APC was funded by the Community of Madrid within the framework of the Multiannual Agreement with the Universidad Politécnica de Madrid in the line of action for the "Programme of Excellence for the University Academic Staff".

Data Availability Statement: The second and third dataset used in this work is provided by the National Renewable Energy Laboratory. They are freely available at http://www.nrel.gov/midc/oahu_archive/ (accessed on 2 June 2024) and https://midcdmz.nrel.gov/apps/day.pl?UOSMRL (accessed on 2 June 2024).

Conflicts of Interest: The authors declare no conflicts of interest.

References

1. Yang, D.; Wang, W.; Gueymard, C.A.; Hong, T.; Kleissl, J.; Huang, J.; Perez, M.J.; Perez, R.; Bright, J.M.; Xia, X.; et al. A review of solar forecasting, its dependence on atmospheric sciences and implications for grid integration: Towards carbon neutrality. *Renew. Sustain. Energy Rev.* **2022**, *161*, 112348. [CrossRef]
2. Gallego, C.; Cuerva, Á.; Costa, A. Detecting and characterising ramp events in wind power time series. *J. Phys. Conf. Ser.* **2014**, *555*, 12040. [CrossRef]
3. Yan, H.W.; Liang, G.; Beniwal, N.; Rodriguez, E.; Farivar, G.G.; Pou, J. Flexible Power Point Tracking Aided Power Ramp Rate Control for Photovoltaic Systems With Small Energy Storage Capacity. *IEEE Trans. Power Electron* **2024**, *39*, 2798–2810. [CrossRef]
4. Cirés, E.; Marcos, J.; de la Parra, I.; García, M.; Marroyo, L. The potential of forecasting in reducing the LCOE in PV plants under ramp-rate restrictions. *Energy* **2019**, *188*, 116053. [CrossRef]
5. Abuella, M.; Chowdhury, B. Forecasting of solar power ramp events: A post-processing approach. *Renew. Energy* **2019**, *133*, 1380–1392. [CrossRef]
6. Wellby, S.J.; Engerer, N.A. Categorizing the Meteorological Origins of Critical Ramp Events in Collective Photovoltaic Array Output. *J. Appl. Meteorol. Climatol* **2016**, *55*, 1323–1344. [CrossRef]
7. Abuella, M.; Chowdhury, B. Forecasting Solar Power Ramp Events Using Machine Learning Classification Techniques. In Proceedings of the 2018 9th IEEE International Symposium on Power Electronics for Distributed Generation Systems (PEDG), Charlotte, NC, USA, 25–28 June 2018; pp. 1–6. [CrossRef]
8. Cui, M.; Zhang, J.; Feng, C.; Florita, A.R.; Sun, Y.; Hodge, B.-M. Characterizing and analyzing ramping events in wind power, solar power, load, and netload. *Renew. Energy* **2017**, *111*, 227–244. [CrossRef]
9. Eltohamy, M.S.; Moteleb, M.S.A.; Talaat, H.E.A.; Mekhamer, S.F.; Omran, W.A. A novel approach for power ramps classification in wind generation. *Sci. Rep.* **2023**, *13*, 1–26. [CrossRef] [PubMed]
10. Chen, X.; Du, Y.; Lim, E.; Wen, H.; Jiang, L. Sensor network based PV power nowcasting with spatio-temporal preselection for grid-friendly control. *Appl. Energy* **2019**, *255*, 113760. [CrossRef]
11. Logothetis, S.-A.; Salamalikis, V.; Nouri, B.; Remund, J.; Zarzalejo, L.F.; Xie, Y.; Wilbert, S.; Ntavelis, E.; Nou, J.; Hendrikx, N.; et al. Solar Irradiance Ramp Forecasting Based on All-Sky Imagers. *Energies* **2022**, *15*, 6191. [CrossRef]
12. Müllner, D. Modern Hierarchical, Agglomerative Clustering Algorithms. *arXiv* **2011**, arXiv:1109.2378. [CrossRef]
13. Reno, M.J.; Hansen, C.W. Identification of periods of clear sky irradiance in time series of GHI measurements. *Renew. Energy* **2016**, *90*, 520–531. [CrossRef]
14. Fernando, D.M.Z.; Calça, M.V.C.; Noris, F.J.; Raniero, M.R.; Pai, A.D. Classification of Sky Cover by the Clearness Index (Kt) in Maputo—Mozambique. *Res. Soc. Dev.* **2022**, *11*, e20611628887. [CrossRef]
15. Suárez-García, A.; Díez-Mediavilla, M.; Granados-López, D.; González-Peña, D.; Alonso-Tristán, C. Benchmarking of meteorological indices for sky cloudiness classification. *Sol. Energy* **2020**, *195*, 499–513. [CrossRef]
16. Alves, M.d.C.; Sanches, L.; Nogueira, J.d.S.; Silva, V.A.M. Effects of Sky Conditions Measured by the Clearness Index on the Estimation of Solar Radiation Using a Digital Elevation Model. *Atmos. Clim. Sci.* **2013**, *3*, 618–626. [CrossRef]
17. Gueymard, C.A.; Bright, J.M.; Lingfors, D.; Habte, A.; Sengupta, M. A posteriori clear-sky identification methods in solar irradiance time series: Review and preliminary validation using sky imagers. *Renew. Sustain. Energy Rev.* **2019**, *109*, 412–427. [CrossRef]
18. Blanc, P.; Wald, L. The SG2 algorithm for a fast and accurate computation of the position of the Sun for multi-decadal time period. *Sol. Energy* **2012**, *86*, 3072–3083. [CrossRef]
19. Perpiñán, O.; Marcos, J.; Lorenzo, E. Electrical power fluctuations in a network of DC/AC inverters in a large PV plant: Relationship between correlation, distance and time scale. *Sol. Energy* **2013**, *88*, 227–241. [CrossRef]
20. IDe la Parra, I.; Marcos, J.; García, M.; Marroyo, L. Control strategies to use the minimum energy storage requirement for PV power ramp-rate control. *Sol. Energy* **2015**, *111*, 332–343. [CrossRef]
21. Vignola, F.; Andreas, A. *University of Oregon: GPS-based Precipitable Water Vapor (Data)*; NREL Report No. DA-5500-64452; NREL-DATA (National Renewable Energy Laboratory-Data (NREL-DATA)): Golden, CO, USA, 2013. [CrossRef]
22. Segupta, M.; Andreas, A. *Oahu Solar Measurement Grid (1-Year Archive): 1-Second Solar Irradiance*; U.S. Department of Energy: Oahu, HI, USA, 2010. [CrossRef]
23. Journée, M.; Bertrand, C. Quality control of solar radiation data within the RMIB solar measurements network. *Sol. Energy* **2011**, *85*, 72–86. [CrossRef]
24. Yang, D.; Ye, Z.; Lim, L.H.I.; Dong, Z. Very short term irradiance forecasting using the lasso. *Sol. Energy* **2015**, *114*, 314–326. [CrossRef]
25. Pedregosa, F.; Varoquaux, G.; Gramfort, A.; Michel, V.; Thirion, B.; Grisel, O.; Blondel, M.; Prettenhofer, P.; Weiss, R.; Dubourg, V.; et al. Scikit-learn: Machine Learning in Python. *J. Mach. Learn. Res.* **2011**, *12*, 2825–2830.
26. Hoff, T.E.; Perez, R. Quantifying PV power Output Variability. *Sol. Energy* **2010**, *84*, 1782–1793. [CrossRef]

27. Mills, A.; Wiser, R. *Implications of Wide-Area Geographic Diversity for Short-Term Variability of Solar Power*; U.S. Department of Energy: Oahu, HI, USA, 2010; Available online: https://escholarship.org/uc/item/9mz3w055 (accessed on 23 February 2024).
28. Remund, J.; Calhau, C.; Perret, L.; Marcel, D. *Characterization of the Spatio-Temporal Variations and Ramp Rates of Solar Radiation and PV Report of IEA Task 14 Subtask 1.3*; International Energy Agency: Paris, France, 2015; Available online: https://iea-pvps.org/key-topics/characterization-of-the-spatio-temporal-variations-and-ramp-rates-of-solar-radiation-and-pv-2015/ (accessed on 4 May 2022).
29. Wiemken, E.; Beyer, H.; Heydenreich, W.; Kiefer, K. Power characteristics of PV ensembles: Experiences from the combined power production of 100 grid connected PV systems distributed over the area of Germany. *Sol. Energy* **2001**, *70*, 513–518. [CrossRef]
30. Hoff, T.E.; Perez, R. Modeling PV fleet output variability. *Sol. Energy* **2012**, *86*, 2177–2189. [CrossRef]
31. Marcos, J.; Marroyo, L.; Lorenzo, E.; García, M. Smoothing of PV power fluctuations by geographical dispersion. *Prog. Photovoltaics Res. Appl.* **2012**, *20*, 226–237. [CrossRef]
32. Perpiñán, O.; Lorenzo, E. Analysis and synthesis of the variability of irradiance and PV power time series with the wavelet transform. *Sol. Energy* **2011**, *85*, 188–197. [CrossRef]
33. Marcos, J.; Marroyo, L.; Lorenzo, E.; Alvira, D.; Izco, E. From irradiance to output power fluctuations: The PV plant as a low pass filter. *Prog. Photovoltaics Res. Appl.* **2011**, *19*, 505–510. [CrossRef]
34. Uruel-Sanz, J.; Perpiñán-Lamigueiro, O. Power Flow Analysis in Urban Distribution Networks with Implementation of Grid-Connected Photovoltaic Systems. *Solar* **2022**, *2*, 32–51. [CrossRef]